A new efficient method to solve the stream power law model taking into account sediment deposition

Xiaoping P. Yuan, Jean Braun, Laure Guerit, Delphine Rouby, Guillaume Cordonnier

A new efficient method to solve the stream power law model taking into account sediment deposition

X. P. Yuan[1], J. Braun[1,2], L. Guerit[3], D. Rouby[3], and G. Cordonnier[4]

[1]Helmholtz Centre Potsdam, German Research Centre for Geosciences (GFZ), Potsdam, Germany
[2]Institute of Earth and Environmental Sciences, University of Potsdam, Potsdam, Germany
[3]Géosciences Environnement Toulouse, UMR5563 CNRS-IRD-Université de Toulouse, France
[4]Ecole polytechnique, Palaiseau, France

Key Points:

- We present an efficient ($O(N)$ and implicit) method to solve a river erosion model taking into account sediment deposition.
- We show how the foreland stratigraphy is controlled by the efficiency of river erosion and the efficiency of sediment transport by rivers.
- We observe autogenic aggradation and incision cycles in the foreland once the system reaches a dynamic steady state.

Corresponding author: X. P. Yuan, xyuan@gfz-potsdam.de

Abstract

The stream power law model has been widely used to represent erosion by rivers, but does not take into account the role played by sediment in modulating erosion and deposition rates. *Davy and Lague* (2009) provide an approach to address this issue, but it is computationally demanding because the local balance between erosion and deposition depends on sediment flux resulting from net upstream erosion. Here, we propose an efficient (i.e., $O(N)$ and implicit) method to solve their equation. This means that, unlike other methods used to study the complete dynamics of fluvial systems (including the transition from detachment-limited to transport-limited behavior, for example), our method is unconditionally stable even when large time steps are used. We demonstrate its applicability by performing a range of simulations based on a simple setup composed of an uplifting region adjacent to a stable foreland basin. As uplift and erosion progress, the mean elevations of the uplifting relief and the foreland increase, together with the average slope in the foreland. Sediments aggrade in the foreland and prograde to reach the base level where sediments are allowed to leave the system. We show how the topography of the uplifting relief and the stratigraphy of the foreland basin are controlled by the efficiency of river erosion and the efficiency of sediment transport by rivers. We observe the formation of a steady-state geometry in the uplifting region, and a dynamic steady state (i.e., autocyclic aggradation and incision) in the foreland, with aggradation and incision thicknesses up to tens of metres.

1 Introduction

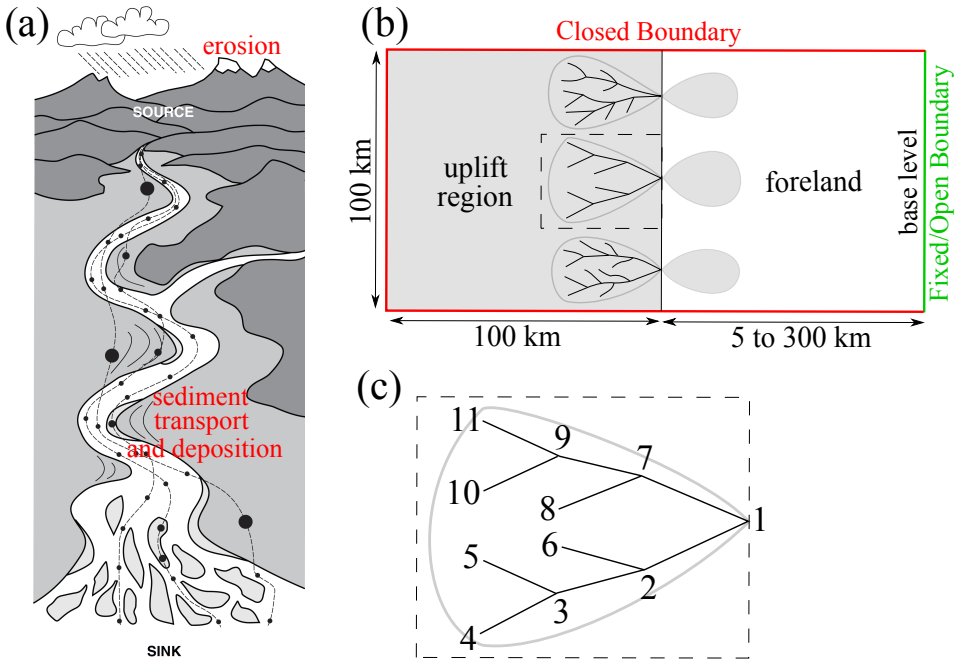

Figure 1. (a) The concept of source to sink with sediment transport and deposition, modified from *Allen and Heller* (2011). (b) Setup for our simulation with uplifting region and foreland basin. (c) Illustration of a simple catchment with normal FastScape stack order (*Braun and Willett*, 2013). In (b), the red lines indicate the closed boundary where sediment flux cannot leave the system, whereas base level (green line) is fixed as an open boundary.

Quantifying the dynamics of river erosion, sediment transport and deposition (Figure 1a) is a fundamental problem in geomorphology that has great relevance for our understanding of landscape evolution in tectonically active areas. Many parameterizations of these processes have been proposed and implemented in numerical landscape evolution models (*Braun and Sambridge*, 1997; *Chase*, 1992; *Crave and Davy*, 2001; *Kooi and Beaumont*, 1994; *Tucker and Slingerland*, 1994).

The Stream Power Law (SPL) model has been widely used to represent erosion by rivers (*Howard and Kerby*, 1983; *Whipple and Tucker*, 1999). In its simplest form, it assumes that erosion rate is proportional to the shear stress exerted by the river on its bed which, in turn, is proportional to net precipitation rate, p, drainage area, A, and local slope, S, according to:

$$\frac{\partial h}{\partial t} = U - K_f\, p^m A^m S^n\,, \tag{1}$$

where h is topographic elevation, t is time, U is uplift rate, K_f is the fluvial erosion coefficient, and m and n are the SPL exponents. An important assumption of the SPL model is that sediments are efficiently transported by rivers and not deposited in the simulated domain. The SPL model has been shown to describe a number of fluvial landscapes and processes. It is for example commonly used to infer uplift pattern from river profiles or to model topographic evolution at the scale of a catchment (*Braun and Willett*, 2013; *Campforts et al.*, 2017; *Lavé and Avouac*, 2001). Yet, it is well known that this model might be oversimplified as it does not consider several important processes acting in river channels (*Lague*, 2014). In particular, it is necessary to take into account the role played by sediment in modulating erosion rate and/or deposition (*Whipple and Tucker*, 2002), such as a dependence on bedload transport (*Davy and Lague*, 2009; *Kooi and Beaumont*, 1994) or a bed-cover effect (*Cowie et al.*, 2008; *Johnson et al.*, 2009; *Sklar and Dietrich*, 2001). In fact, transported sediments provide the tools for abrasion and fracturing of rock but also, if overly abundant, they can protect the bedrock from erosion (*Sklar and Dietrich*, 1998).

Several parameterizations have been proposed to adapt the SPL model to incorporate the effects of transported sediments, including the erosion-deposition formulation proposed by *Davy and Lague* (2009), which differs from models based on the divergence of sediment flux (e.g., *Paola and Voller*, 2005) in that it conserves mass on the bed and in the water column to treat simultaneous erosion and deposition of a single substrate (*Shobe et al.*, 2017). Based on previous erosion-deposition models (e.g., *Beaumont et al.*, 1992; *Kooi and Beaumont*, 1994), *Davy and Lague*'s (2009) formulation has a limited number of parameters, while attempting to relate these parameters to physical processes and quantities (e.g., saltation length). In addition, their erosion-deposition framework allows the exploration of both detachment-limited and transport-limited models with simple parameter changes, and displays a smooth transition between the two types of model behavior.

Davy and Lague's (2009) formulation has been used or adapted to obtain simple models (e.g., *Carretier et al.*, 2016; *Ganti et al.*, 2014; *Langston and Tucker*, 2018; *Mouchené et al.*, 2017; *Shobe et al.*, 2017), which assume that the net rate of topographic change is the sum of the erosion rate (controlled by the SPL model) and of the deposition rate, which is proportional to local suspended sediment flux and to a dimensionless deposition coefficient, and inversely proportional to drainage area, a proxy for water discharge. This parameterization is also receiving growing acceptance due to its ability to reproduce many depositional features of fluvial systems (*Carretier et al.*, 2016; *Mouchené et al.*, 2017; *Shobe et al.*, 2017). However, because the local balance between erosion and deposition depends on sediment flux resulting from net upstream erosion, this parameterization is computationally demanding.

Braun and Willett (2013) have proposed an efficient algorithm for solving the SPL model, which is ideally suited for a large number of model simulations as required for

inverting observational constraints in a Bayesian approach. Here we present an equally efficient (i.e., $O(N)$ and implicit) method to solve the equation proposed by *Davy and Lague* (2009) that takes into account sediment deposition. $O(N)$ means that the computational time increases linearly with the number of points used to discretize the landscape. An implicit scheme guarantees unconditionally stable time integration of the landscape evolution equation, which means that large time steps can be used without affecting numerical stability. This is potentially an important step as it allows one to use sedimentological observations, such as the stratigraphy of foreland basins or the position and thickness of river terraces, to further constrain landscape evolution models.

Nonetheless, the novelty of our study is not limited to the description of the computational efficiency. Based on this algorithm, our model can simulate erosion and deposition in fluvial landscapes, at large spatial (up to thousands of kilometers) and temporal (up to tens of millions of years) scales. Because these two processes are considered in one single equation, deposition can occur anywhere in the domain (i.e., not only in depressed areas but also along channels or in stable continental areas). We therefore use our new algorithm to explore the impact of coupling erosion and deposition in a fluvial landscape, and show that this erosion-deposition relationship, which is often ignored, has a strong impact on relief in the uplifted domain, the concavity of the channels and their steepness index. We also demonstrate that this relatively simple model leads to the cyclic formation and destruction of river banks as the stream continuously migrates and sometimes erodes into the sediment it has previously deposited. Such autogenic aggradation and incision cycles are currently difficult to simulate in landscape evolution models. The simulations using the new model can thus improve our understanding of the links between external forcings, internal processes, and depositional features.

In the next section, we first present our implementation of *Davy and Lague*'s (2009) model and the $O(N)$ and implicit numerical scheme. Model implications of our new formulation are shown in Section 3. We then explore the model behavior in Section 4 by performing a range of simulations based on a simple setup composed of an uplifting region adjacent to a stable continental area on which a foreland basin develops. In Section 5, using our model, we observe the formation of autocyclic aggradation and incision in the foreland once the system reaches a dynamic steady state.

2 Model implementation

2.1 SPL model taking into account sediment deposition

The effect of upstream sediment flux was first incorporated into the SPL model by *Kooi and Beaumont* (1994), by assuming that the rate of topographic change results from the imbalance between a sediment "carrying capacity", q_f^{eqb}, and the upstream sediment yield, q_s, according to:

$$\frac{\partial h}{\partial t} = U - \frac{1}{L_f}\left(q_f^{eqb} - q_s\right) \quad \text{with} \quad q_f^{eqb} = K\, q_w\, S\,, \tag{2}$$

where L_f is a transport length, K is a dimensionless erosion coefficient, $q_w = Q_w/W$ is water discharge per unit width (Q_w, water discharge, and W, river width), and q_s is the sediment flux per unit width obtained by integrating the net upstream erosion rate:

$$q_s = \frac{1}{W}\int_A \left(U - \frac{\partial h}{\partial t}\right) dA\,. \tag{3}$$

This sediment flux therefore accounts for the whole solid load (bed, suspended, and wash load). The transport length L_f in (2) can be regarded as the length scale over which the imbalance between the upstream sediment yield and the river carrying capacity is resolved either by deposition (in cases where the river is over-capacity) or by erosion (in cases where the river is under-capacity). Physically, L_f represents the average transport distance of

sediment grains within the flow from the location where they are eroded to the location where they are deposited (*Beaumont et al.*, 1992). L_f thus characterizes the proportion of incoming sediment flux which is deposited (the larger the value of L_f, the lower the rate of deposition).

Combining equations (2) and (3) leads to:

$$\frac{\partial h}{\partial t} = U - \frac{1}{L_f}\Big[\frac{K\,Q_w S}{W} - \frac{1}{W}\int_A \Big(U - \frac{\partial h}{\partial t}\Big) dA\Big]\,. \tag{4}$$

To derive the SPL model, two major assumptions are commonly made. Firstly, it is assumed that river width W varies as the square root of the water discharge (*Lacey*, 1930; *Leopold and Miller*, 1956):

$$W = c\,Q_w^{0.5}\,, \tag{5}$$

where c is an empirical constant, typically of the order of $(0.1{-}1){\times}10^{-2}$ (*Montgomery and Gran*, 2001, and references therein). Secondly, water discharge can be expressed as the product of net precipitation rate p and drainage area A:

$$Q_w = pA = p_0\,\tilde{p}A\,, \tag{6}$$

where p_0 is mean net precipitation rate, and $\tilde{p} = p/p_0$ represents any spatial or temporal variation in precipitation p relative to the mean precipitation p_0. Combining equations (5) and (6) with equation (4) leads to

$$\frac{\partial h}{\partial t} = U - \frac{1}{L_f}\Big[\frac{K\,p_0^{0.5}}{c}\tilde{p}^{0.5}A^{0.5}S - \frac{1}{c\,p_0^{0.5}\,\tilde{p}^{0.5}A^{0.5}}\int_A \Big(U - \frac{\partial h}{\partial t}\Big) dA\Big]\,. \tag{7}$$

The contribution of *Davy and Lague* (2009) can be regarded as an improvement on *Kooi and Beaumont*'s (1994) method in an attempt to relate the transport length L_f to physical parameters (e.g., water discharge and settling velocity of grains within the flow). According to *Davy and Lague*'s (2009) formulation, the rate of change of topographic elevation is given by:

$$\frac{\partial h}{\partial t} = U - K' q_w^{m'} S^{n'} + \frac{q_s}{L_f} = U - K' q_w^{m'} S^{n'} + \frac{d^*\,v_s}{q_w} q_s\,, \tag{8}$$

where K' is an erosion efficiency coefficient, m' and n' are two exponents, v_s is the net settling velocity of sediment grains, and d^* is the ratio between the sediment concentration near the riverbed interface and the average concentration over the water column. The value of $d^*(\geq 1)$ varies as a function of the Rouse number which defines the relative contribution of bed, suspended, and wash loads (*Davy and Lague*'s (2009) Figure 4). *Davy and Lague* (2009) discuss how d^* can be calculated for suspended load and bed load rivers. For small rivers (or large particles), most of the entrainment mechanisms lie in the bed load, d^* is much larger than 1 and the transport length L_f is small. Conversely, for large rivers (or small particles) the Rouse number is small, d^* is close to 1 and L_f is large. *Davy and Lague* (2009) present such a model based on the relative contributions of (i) erosion from the bed into the water column (suspended load) and (ii) deposition from the water column onto the bed. Thus, the transport length L_f takes into account the deposition of the bed load and the suspended load. With this approach, the deposition term is proportional to the ratio between the sediment flux q_s and the water flux q_w. If $q_s \gg q_w$, deposition is high. On the contrary, if $q_s \ll q_w$, the deposition term tends toward 0. Note that both terms are proportional to the drainage area of the catchment.

The equivalent of *Kooi and Beaumont*'s (1994) transport length L_f in the *Davy and Lague*'s (2009) approach is therefore:

$$L_f = \frac{q_w}{d^*\,v_s} = \frac{Q_w}{W d^*\,v_s} = \frac{pA}{W d^*\,v_s} = \frac{p_0\,\tilde{p}A}{W d^*\,v_s} = \frac{\tilde{p}A}{WG}\,, \quad \text{with} \quad G = \frac{d^*\,v_s}{p_0}\,, \tag{9}$$

where G is a dimensionless deposition coefficient, which is a function of the sediment concentration ratio in transport, the settling velocity of sediment, and the mean precipitation rate. $G/\tilde{p}$ is identical to Θ as defined in *Davy and Lague* (2009). They showed that, for typical values of the various parameters ($p = 10^{-7}$ m/s, $v_s \in \left[10^{-6} - 10^{-1}\right]$ m/s), $G/\tilde{p}$ is of order 1 or greater, in good agreement with estimates from natural sedimentary systems (*Guerit et al.* (2018), pers. comm.).

Equations (3), (5), (6) and (9) can be combined with equation (8) to yield:

$$\begin{aligned}\frac{\partial h}{\partial t} &= U - K'\Big(\frac{Q_w}{W}\Big)^{m'} S^{n'} + \frac{1}{WL_f}\int_A \Big(U - \frac{\partial h}{\partial t}\Big)dA \\ &= U - \frac{K'\,p_0^{0.5m'}}{c^{m'}}\tilde{p}^{0.5m'}A^{0.5m'}S^{n'} + \frac{G}{\tilde{p}A}\int_A \Big(U - \frac{\partial h}{\partial t}\Big)dA\,.\end{aligned} \tag{10}$$

In the parametric study of *Davy and Lague* (2009), $m' = n' = 1$ and their erosion term $\frac{K'\,p_0^{0.5}}{c}\tilde{p}^{0.5}A^{0.5}S$ is thus similar to that of *Kooi and Beaumont* (1994). The main differences between their models are: (i) the depositional term is inversely proportional to either the drainage area (*Davy and Lague*, 2009) or the square root of drainage area (*Kooi and Beaumont*, 1994); and (ii) L_f is applied only to q_s (*Davy and Lague*, 2009), or is applied to both q_f^{eqb} and q_s (*Kooi and Beaumont*, 1994).

Replacing $K'\,p_0^{0.5}/c^{m'}$, $0.5m'$ and n' in (10) by K_f, m and n, respectively, we can make a more direct connection to the SPL model and write that the rate of topographic change $\partial h/\partial t$ in response to tectonic uplift, river erosion and sediment deposition is given by:

$$\frac{\partial h}{\partial t} = U - K_f\,\tilde{p}^m A^m S^n + \frac{G}{\tilde{p}A}\int_A \Big(U - \frac{\partial h}{\partial t}\Big)dA\,. \tag{11}$$

The modified SPL formulation has only one additional parameter (i.e., the dimensionless deposition coefficient G) compared to the classic SPL model. The dimensionless constant G multiplying the deposition rate in (11) depends on an assumed mean precipitation rate; any spatial or temporal variation in precipitation rate is introduced through the variable $\tilde{p}$. At steady state, the catchment area A in the deposition term vanishes, and the deposition term is equal to $GU/\tilde{p}$. Note that this modified SPL formulation is constructed by considering fluxes and, therefore, it does not specifically consider the effect of grain size. However, the mathematical definition of G in (9) makes it related to the size of the sediments in transport through the settling velocity v_s. In this work, we consider different values of $G = d^*\,v_s/p_0$ as a whole, rather than studying individually different values of d^*, v_s, and p_0.

Fluvial erosion leads to the formation of hillslopes along river channels. Fluvial erosion and hillslope processes are interdependent, therefore hillslope processes need to be included in our model, which are commonly represented by a linear diffusion term (*Ahnert*, 1967):

$$\frac{\partial h}{\partial t} = K_d\nabla^2 h\,, \tag{12}$$

where K_d is a hillslope sediment transport coefficient. In our model, the diffusion equation (12) is calculated separately, after solving equation (11). Both equations are applied in every cell of the landscape.

Easily detachable materials such as unconsolidated sediments should be characterized by a larger erosion coefficient K_f than bedrock (*Davy and Lague*, 2009; *Kooi and Beaumont*, 1994). Therefore, K_f depends on whether topographic elevation h is higher than basement elevation h_{base} or not. In areas that are in net erosion (i.e., $h \leq h_{base}$), we assume $K_f = K_{fb}$ (subscript $_b$ represents bedrock), whereas in areas covered by sediments (i.e., $h > h_{base}$), we assume $K = K_{fs}$ (subscript $_s$ represents sediments). In most of our simulations, we assume $K_{fb} = K_{fs}$ for the sake of simplicity, and we use $K_{fb} \neq K_{fs}$ for our sensitivity analysis in Section 4.2.2.

175 ### 2.2 $O(N)$ and implicit algorithm

The most challenging part is to solve equation (11) in an efficient manner (i.e., in $O(N)$ operations) and using an implicit algorithm that allows for large time steps. For this we first discretize equation (11) using a backward Euler implicit finite difference scheme for each of the $n_x \times n_y$ nodes (n_x and n_y are the number of nodes to discretize the landscape in the x- and y-directions, respectively) as follows:

$$\frac{h_i^{t+\Delta t} - h_i^t}{\Delta t} = U - K_f\, \tilde{p}^m A_i^m \Big(\frac{h_i^{t+\Delta t} - h_{rec(i)}^{t+\Delta t}}{\Delta l_i}\Big)^n + \frac{G}{\tilde{p}\tilde{A}_i} \sum_{j=ups(i)} \Big(U - \frac{h_j^{t+\Delta t} - h_j^t}{\Delta t}\Big), \quad 1 \le i \le n_x \times n_y\,, \tag{13}$$

in which, h_i^t and $h_i^{t+\Delta t}$ are the elevations of the i-th node at time t and time $t+\Delta t$, respectively, $h_{rec(i)}^{t+\Delta t}$ is the elevation of the i-th node's receiver (the node in the steepest-descent drainage direction of the i-th node) at time $t+\Delta t$, Δl_i is the distance between the i-th node and its receiver, and $\sum_{j=ups(i)}$ represents the sum of the i-th node's upstream catchment nodes. $\tilde{A}_i$ in equation (13) is a dimensionless catchment area defined as:

$$\tilde{A}_i = A_i/(\Delta x \Delta y) = N_i\,, \tag{14}$$

176 where $\Delta x, \Delta y$ are the horizontal sizes of the cells, and N_i is simply the number of cells
177 upstream of cell i. To compute the catchment areas A_i in $O(N)$ operations, we use the
178 reverse stack order as defined in the FastScape algorithm (*Braun and Willett*, 2013).

To explain the remaining parts of our proposed numerical scheme, we assume that $n = 1$. The general case ($n \neq 1$) is dealt with later. When $n = 1$, equation (13) can be expressed as

$$\begin{aligned} &- F_i\, h_{rec(i)}^{t+\Delta t} + (1 + F_i)\, h_i^{t+\Delta t} + \frac{G}{\tilde{p}\tilde{A}_i} \sum_{j=ups(i)} h_j^{t+\Delta t} = b_i^t\,, \\ &\text{with} \quad F_i = \frac{K_f\, \tilde{p}^m A_i^m \Delta t}{\Delta l_i}\,, \quad \text{and} \quad b_i^t = h_i^t + U\Delta t + \frac{G}{\tilde{p}\tilde{A}_i} \sum_{j=ups(i)} (h_j^t + U\Delta t)\,. \end{aligned} \tag{15}$$

179 The term b_i^t on the right-hand side of the equation is known from the solution at time
180 t, while elevations on the left-hand side are unknown at time $t + \Delta t$.

For the nodes at base level (open boundary, Figure 1b), we assume that the elevation is constant through time:

$$h_{base\,level}^{t+\Delta t} = h_{base\,level}^t\,. \tag{16}$$

181 We also assume that sediment can leave the system from these base level nodes.

The above finite difference equations can be expressed in the following matrix form:

$$\underline{\underline{B}} \cdot \underline{h}^{t+\Delta t} = \underline{b}^t\,. \tag{17}$$

As shown in Appendix A, if we use the FastScape stack order in Figure 1c to solve equation (17), every row i of $\underline{\underline{B}}$ has a single non-zero element before the diagonal element that corresponds to the receiver of node i, and many non-zero elements after the diagonal element that correspond to all upstream nodes of i. Solving (17) by factorizing the matrix $\underline{\underline{B}}$ (e.g., by Gauss-Jordan elimination) is a problem of complexity of $O(n^3)$. To obtain a greater efficiency, we use a Gauss-Seidel iteration scheme to compute $\underline{h}^{t+\Delta t}$ in equation (17). This iterative algorithm requires to split the matrix $\underline{\underline{B}}$ into its lower $\underline{\underline{F}}$ and strictly upper triangular matrix $\underline{\underline{E}}$ as follows:

$$\underline{\underline{B}} \cdot \underline{h}^{t+\Delta t} = (\underline{\underline{F}} + \underline{\underline{E}}) \cdot \underline{h}^{t+\Delta t} = \underline{b}^t\,, \tag{18}$$

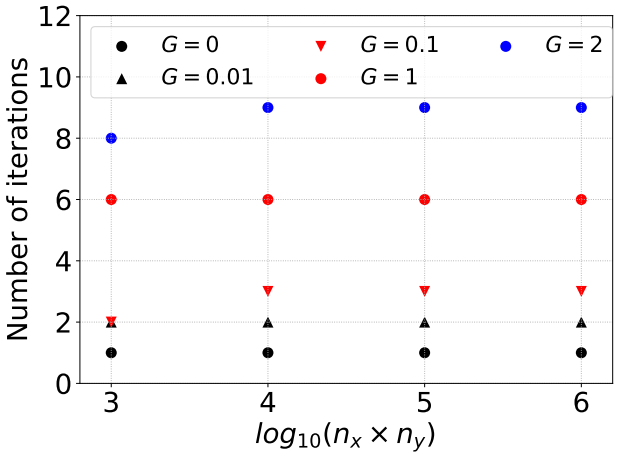

Figure 2. The number of iterations required for the solution to be convergent as a function of resolution $n_x \times n_y$. Solving equation (19) on a square area of resolution $n_x \times n_y = 961, 10000, 99856$, and 1000000, using $U = 0.2$ mm/yr, $K_f = 2 \times 10^{-5}$ m^{1-2m}/yr, $p = 1$ m/yr, and varying the value of G.

where the matrices $\underline{\underline{F}}$ and $\underline{\underline{E}}$ are shown in Appendix A.

The Gauss-Seidel iterative process starts with an initial guess $\underline{h}^{t+\Delta t,\,0} = \underline{h}^t$ and uses the following recurrence to obtain an improved estimate $\underline{h}^{t+\Delta t,\,k+1}$:

$$\underline{\underline{F}} \cdot \underline{h}^{t+\Delta t,\,k+1} = \underline{b}^t - \underline{\underline{E}} \cdot \underline{h}^{t+\Delta t,\,k}\,, \tag{19}$$

from the value $\underline{h}^{t+\Delta t,\,k}$ obtained at the previous iteration. Interestingly, equation (19) can be written in a different form for each node i:

$$h_i^{t+\Delta t,\,k+1} = \frac{b_i^t - G/(\tilde{p}\tilde{A}_i)\sum_{j=ups(i)} h_j^{t+\Delta t,k} + F_i\, h_{rec(i)}^{t+\Delta t,\,k+1}}{1+F_i}\,, \tag{20}$$

if the nodes are processed in the FastScape stack order.

The procedure is continued until the maximum difference in node elevation between two successive iterations is below a given tolerance ϵ (expressed in meters) as

$$\max|h_i^{t+\Delta t,k+1} - h_i^{t+\Delta t,k}| < \epsilon \quad \text{for all } i \text{ such that } 1 \leq i \leq n_x \times n_y\,. \tag{21}$$

The tolerance is taken as a small fraction (10^{-3}) of the increment in topography, $U\Delta t$.

The above procedure based on a Gauss-Seidel iterative scheme is known to converge if the matrix $\underline{\underline{B}}$ is strictly diagonally dominant: $|-F_i| + |\sum_{j=ups(i)} G/(\tilde{p}\tilde{A}_i)| < |1+F_i|$, thus $G/\tilde{p} < N_i/(N_i-1)$ after some derivations. Therefore, the iterative method is proven to converge unconditionally at least when $G/\tilde{p} \leq 1$, but we show experimentally in section 4 that this method can also converge even if this condition is not satisfied.

As shown in Figure 2, our new implicit method to solve equation (13) is $O(N)$ as the number of iterations required in the Gauss-Siedel scheme depends on the value of G but not on the resolution of the model ($n_x \times n_y$).

We note that the left-hand side of equation (19) is the same as in the FastScape algorithm (*Braun and Willett*, 2013) while the right-hand side only differs by a single

196 term given by: $\underline{\underline{E}} \cdot \underline{h}^{t+\Delta t,\,k}$ at time $t+\Delta t$. The implementation of our new algorithm
197 is therefore a very simple addition to the FastScape algorithm. Note also that, if the value
198 of the deposition coefficient G is null, the right-hand side term simplifies to $\underline{b}^t$, and the
199 new algorithm is identical to the basic FastScape algorithm which does not require the
200 Gauss-Seidel iteration to obtain the elevation at time $t+\Delta t$.

The above Gauss-Seidel iteration algorithm can be extended to consider different values of K_f and G to differentiate between bedrock and previously deposited sediments during the iteration process. Basement elevation $h_{base}^{t+\Delta t}$ at each step is obtained using:

$$h_{base}^{t+\Delta t} = \min(h^{t+\Delta t}, h_{base}^{t} + U\Delta t)\,, \tag{22}$$

201 where $h_{base}^{t}+U\Delta t$ is the basement elevation resulting from uplift without surface pro-
202 cesses.

When the value of n is not equal to 1, equation (13) becomes:

$$h_i^{t+\Delta t,\,k+1} + K_f\,\tilde{p}^m A_i^m \Delta t \Big(\frac{h_i^{t+\Delta t,\,k+1} - h_{rec(i)}^{t+\Delta t,\,k+1}}{\Delta l_i}\Big)^n = h_i^t + U\Delta t + \frac{G}{\tilde{p}\tilde{A}_i} \sum_{j=ups(i)} (h_j^t + U\Delta t - h_j^{t+\Delta t,\,k})\,. \tag{23}$$

203 This non-linear equation can be solved by combining the Gauss-Seidel iterations with
204 a local Newton scheme. We solve the diffusion equation (12) using an alternating direc-
205 tion implicit and $O(N)$ scheme (*Peaceman and Rachford*, 1955).

206 3 Model implications on geomorphological relationships

207 Before studying the behaviour of the numerical scheme presented above, we first
208 wish to derive several basic geomorphological relationships from the evolution equation
209 (11). These include the steady-state slope-area relationship, the shape of steady-state
210 river profile, and the expression for the response time (i.e., the time necessary to reach
211 steady state). In this section, all relationships are for the uplifting region only, and we
212 neglect the hillslope processes.

213 3.1 Steady-state slope-area ($S-A$) relationship

At steady state (i.e., when uplift is balanced by channel incision assumed to be governed by the SPL model), the slope and intercept of the relationship between slope and drainage area provide constraints on the concavity (the ratio m/n) and the steepness index ($k_s = (U/K_f)^{1/n}\tilde{p}^{-m/n}$), respectively (e.g., *Wobus et al.*, 2006, and references therein). When taking deposition into account, the SPL model must be replaced by equation (11), which, under the assumption of steady state (i.e., $\frac{\partial h}{\partial t} = 0$) leads to the following slope-area ($S-A$) relationship:

$$S = \Big[\frac{(1+G/\tilde{p})U}{K_f}\Big]^{1/n} A^{-m/n}\tilde{p}^{-m/n} = (1+G/\tilde{p})^{1/n}(U/K_f)^{1/n} A^{-m/n}\tilde{p}^{-m/n}\,. \tag{24}$$

From this equation, a new steepness index can be defined:

$$k_s' = (1+G/\tilde{p})^{1/n}(U/K_f)^{1/n}\tilde{p}^{-m/n}\,, \tag{25}$$

214 that only differs by a factor $(1+G/\tilde{p})^{1/n}$. For typical values of $G/\tilde{p} = 1$ (*Davy and*
215 *Lague*, 2009) and $n = 1$ (*Whipple and Tucker*, 1999), the effect of sediment deposition
216 is to increase the steepness index by a factor of 2.

217 3.2 Steady-state river profile

At steady state, a power-law relationship is generally observed between the length of a stream, x, and its upstream drainage area (*Hack*, 1957; *Lague et al.*, 2003; *Montgomery and Dietrich*, 1992; *Morisawa*, 1962; *Walcott and Summerfield*, 2009) that can

be expressed as:

$$A = k\,x^{b}\,, \tag{26}$$

where k and b, usually close to 0.5 and 2, respectively, are called Hack's law coefficients. Combining equation (26) with equation (24) leads to:

$$S = \frac{dh}{dx} = (1+G/\tilde{p})^{1/n} U^{1/n} K_f^{-1/n} \tilde{p}^{-m/n} k^{-m/n} x^{-\frac{bm}{n}}\,. \tag{27}$$

By integrating the above equation over the length of the stream, we obtain the steady-state river profile:

$$h(x) = (1+G/\tilde{p})^{1/n} U^{1/n} K_f^{-1/n} \tilde{p}^{-m/n} k^{-m/n} (1-\frac{bm}{n})^{-1} x^{1-\frac{bm}{n}} + C\,, \quad \text{for} \quad bm \neq n\,, \tag{28}$$

where $C = 0$ if the elevation at base level is zero (i.e., $h(0) = 0$). We see that the steady-state elevation of every point along the river profile is $(1+G/\tilde{p})^{1/n}$ times higher than what is expected from the classic SPL model (i.e., without sediment deposition).

3.3 Response time

The response time of a fluvial landscape can be defined as the time needed for river profiles to reach steady state. In our model, the response time is

$$\tau' = h(L)/U = (1+G/\tilde{p})^{1/n} U^{1/n-1} K_f^{-1/n} \tilde{p}^{-m/n} k^{-m/n} (1-\frac{bm}{n})^{-1} L^{1-\frac{bm}{n}}\,, \tag{29}$$

where L is the length of the uplifting region. In the classic SPL form (without the term of deposition), the response time of a fluvial landscape is (*Whipple*, 2001)

$$\tau = U^{1/n-1} K_f^{-1/n} \tilde{p}^{-m/n} k^{-m/n} (1-\frac{bm}{n})^{-1} L^{1-\frac{bm}{n}}\,. \tag{30}$$

The ratio between these two response times is once again given by:

$$\frac{\tau'}{\tau} = (1+G/\tilde{p})^{1/n}\,. \tag{31}$$

The impact of continental deposition on the evolution of a fluvial landscape is highlighted by the three geomorphological relationships above: steady-state slope is higher, average topography in the uplifting region is higher, and response time is longer than with the classic SPL model (i.e., without deposition). However, neither the shape of the river profile, nor the dependency of the response time or the steepness index to other parameters (such as K_f, m and n, or the length of the channel, precipitation rate or the uplift rate) are affected by sediment deposition. The dimensionless deposition coefficient G alone controls the difference with respect to the classic SPL model and appears only inside a multiplying factor, $(1+G/\tilde{p})^{1/n}$. In all three relationships we derived above, the factor $(1+G/\tilde{p})^{1/n}$ multiplies the other poorly constrain factor $K_f^{-1/n}$; this means that the effect of sediment deposition (on most morphometric measures and scales) can be included in the SPL erosion coefficient K_f by simply redefining this constant in the following way:

$$K_f' = K_f/(1+G/\tilde{p})\,. \tag{32}$$

This also means that the value of the constant G cannot be easily derived from the concavity of rivers, the total relief of river channels or the response time of fluvial erosion.

4 Model behavior

We now demonstrate the behavior and applicability of our numerical implementation of the modified SPL model by performing a range of simulations. These simulations are based on a simple setup composed of an uplifting region adjacent to a stable

Table 1. Parameters for the simulations.

Notation	Definition	Values/Range	Unit
h	elevation of topography		m
h_{base}	elevation of basement		m
t	time	10	Myr
Δt	incremental time	1000	yr
x	horizontal dimension	105 to 400	km
y	horizontal dimension	100	km
$\Delta x, \Delta y$	cell size	1	km
U	uplift rate	0.2, 0.5, 1	mm/yr
p	net precipitation rate	0.5, 1, 2	m/yr
p_0	mean net precipitation rate	1	m/yr
$\tilde{p} = p/p_0$	variation ratio of precipitation rate	0.5, 1, 2	-
A	drainage area		m^2
S	surface slope in drainage direction		-
m	SPL exponent	0.4^a	-
n	SPL exponent	1^b	-
K_{fb}	SPL erosion coefficient of bedrock	$2 \times 10^{-5\ c}$	m^{1-2m}/yr
K_{fs}	SPL erosion coefficient of sediments	$(2, 4, 8) \times 10^{-5}$	m^{1-2m}/yr
G	deposition coefficient	$(0, 0.1, 1, 10)^d$	-
K_d	hillslope diffusion coefficient	0.01^e	m^2/yr

[a]Parameters from *Stock and Montgomery* (1999) and *Perron et al.* (2009); [b]parameters from *Braun and Willett* (2013); *Stock and Montgomery* (1999); *Whipple and Tucker* (1999) and *Braun and Willett* (2013); [c]parameters from *Whipple and Tucker* (1999); [d]parameters from *Davy and Lague* (2009); [e]parameters from *Densmore et al.* (2007) and *Armitage et al.* (2013).

continental area on which a foreland basin is allowed to develop. Setup for the simulations is a rectangular area of (105 to 400)×100 km^2 (Table 1, Figure 1b). The initial topography has random noise elevation of up to 1 m. This domain is discretized into a number of cells with a cell size of $\Delta x = \Delta y = 1$ km. The left-hand side of the domain (100× 100 km^2) is uplifted at a constant rate U while the foreland is fixed, and the foreland edge (base level) through which the sediments can leave the system is also fixed. We use a constant diffusion coefficient of $K_d = 0.01$ m^2/yr in all simulations. The net mean precipitation rate p_0 is set to 1 m/yr. We perform a series of model runs for a total time of 10 Myr (10 000 time steps of duration 1000 yr) (Table 1).

4.1 Simulations without foreland

We first performed a series of simulations without the foreland to better illustrate the effect of sediment deposition. We run a simulation with $U = 0.2$ mm/yr, $K_f = 2\times 10^{-5}$ $m^{0.2}/yr$, $p = 1$ m/yr and $G = 0$ to test the classic SPL model without sediment deposition. During the experiment, topography rises, and after 4 Myr, reaches steady state. The final simulated landscape is shown in Figure 3a and the evolution of the mean elevation is presented in Figure 3b. As observed from the black curve ($G = 0$, Figure 3b), the mean elevation in the uplifting region increases progressively before decreasing, and then reaches a constant value at steady state. The same behavior is observed in *Davy and Lague*'s (2009) detachment-limited simulations (their Figure 1). Note that this non-monotonous evolution of the mean elevation is probably related to the presence of local minima which are important at the beginning because we start with an initial topography that has random noise. Local minima are known to artificially reduce the erosional

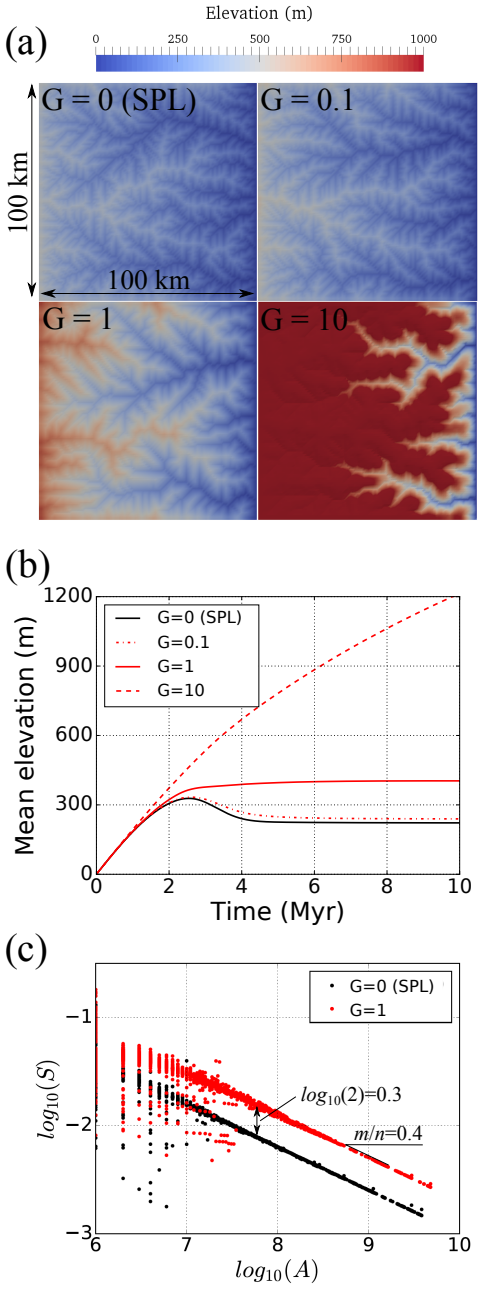

Figure 3. (a) Simulated, plan view topography of the uplifting region for four values of $G = 0, 0.1, 1$, and 10, at 10 Myr. $G = 0$ corresponds with the classic SPL model without taking into account sediment deposition. (b) Mean elevation of uplifting region as a function of time for the four G values. (c) $\log_{10}(S)$ as a function of $\log_{10}(A)$ in steady-state uplifting region for $G = 0$ (SPL model) and 1. We observe that the concavity is $m/n = 0.4$, and the difference in steepness index k_s is by a factor of 2.

efficiency of landscape evolution models by preventing some river discharge to reach downstream locations.

On the contrary, a peak in elevation is not observed in experimental models such as in *Babault et al.* (2005) where they study the development of relief by submitting a thick layer of silica powder to uplift and runoff-driven erosion. In their experiments, the mean elevation increases monotonously before stabilizing around a constant value (their Figure 2A). We suggest that the difference between the two behaviors is due to sediment deposition. To prove this point, we run simulations with $G = 0.1$, 1, and 10. Physically, the larger G, the more deposition in the river channels. The final landscape for the cases of $G = 0.1, 1$, and 10 are compared in Figure 3a. The two simulations with $G = 0$ and $G = 0.1$ are very similar to each other (Figure 3a), but the topography changes significantly if the value of G is ≥ 1. As demonstrated by *Davy and Lague* (2009), the value of $G/\tilde{p} = 1$ corresponds to the transition from detachment-limited to transported-limited behavior.

In terms of average topography, the larger G, the higher the mean elevation (Figure 3b). For $G = 0.1$, only slight differences in mean elevation can be observed with respect to the $G = 0$ simulation (Figure 3b) and steady-state elevation is reached after $\sim$ 4 Myr. On the contrary, the mean elevation for $G = 1$ increases continuously for $\sim 6-7$ Myr before reaching a constant elevation of ~ 400 m, which is almost twice higher than the classic SPL model simulation ($G = 0$) (Figure 3b). This results agrees with our estimate of the response time for fluvial systems including the effect of sediment deposition. When $G \geq 1$, the evolution of the mean elevation is consistent with the one observed in the experiments by *Babault et al.* (2005). As expected from equations (28) and (31), the average elevation at steady state and the response time of the landscape are $(1 + G/\tilde{p})$ times larger when sediment deposition is considered with respect to the classic SPL model. For the case of $G = 10$ (Figure 3b), the mean elevation increases substantially but it does not reach steady state over 10 Myr of simulation. If the model run is allowed to last for a longer period, it should reach steady state after approximately 40 Myr, based on equation (31).

The similarities between laboratory experimental landscapes and our simulations with $G > 0$ confirm that a term for the effect of sediment is required to accurately describe the evolution of a fluvial landscape: although bedrock erosion is the dominant process in the uplifted region (i.e., no net deposition takes place anywhere), the reduction in erosion rate due to sediment deposition, the so-called "cover effect", is key to capture landscape evolution (*Sklar and Dietrich*, 1998; *Whipple and Tucker*, 2002).

4.2 Simulations with foreland sedimentation

4.2.1 Reference simulation

We run a "reference simulation" that includes the presence of a foreland (i.e., a region where $U = 0$). In this reference experiment, the erosion coefficients for bedrock and sediments are first set to the same value for the sake of simplicity (i.e., $K_{fb} = K_{fs} = K_f$). The value of K_f is set to 2×10^{-5} m$^{0.2}$/yr, identical to the one used in the previous set of experiments without a foreland, and G is set to 1. The uplift rate is set to $U = 0.2$ mm/yr, the precipitation rate to $p = 1$ m/yr, and the foreland length to 50 km. The landscape evolution through time and the axial stratigraphy of the resulting foreland basin, with a synthetic stratigraphic layer generated each Myr, are presented in Figure 4a. The associated animations Movie S1 and Movie S2 are presented in the Supporting Information.

At the outlets of the catchments that drain the uplifting region, we observe the formation of small sedimentary fans that progressively coalesce into larger ones. This fan-like deposition is the result of using the SPL model with sediment deposition. As up-

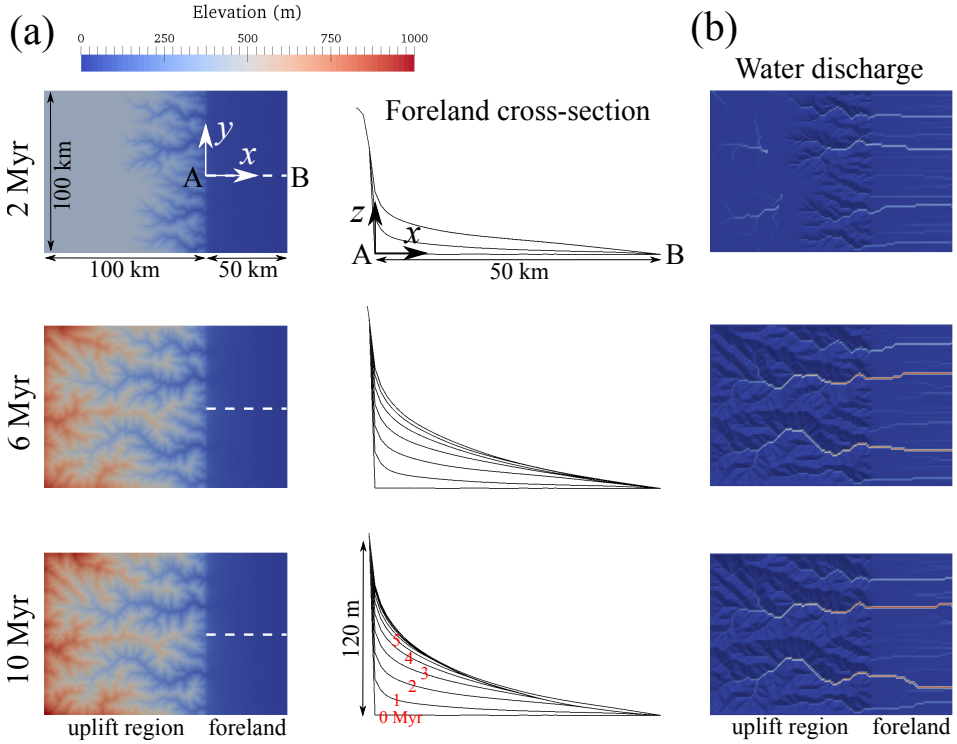

Figure 4. (a) Map view of landscape evolution and longitudinal profile of the central foreland topography (white dashed line in a), and (b) water discharge (the warmer the color, the larger the water discharge) at 2 Myr, 6 Myr, and 10 Myr. See also Movie S1 for landscape evolution, Movie S2 for foreland central cross-section, and Movie S3 for water discharge (lateral variation of river channels in foreland). In (a), the foreland develops a dynamic steady state with the continuous formation and destruction of the riverbeds.

lift and erosion progress, the fans prograde to reach the base level at the far edge of the foreland where the sediments are allowed to leave the system.

The mean elevation of the uplifting region, the maximum thickness of sediments, and the mean surface slope of the foreland basin as function of time are shown by solid curves in Figures 5a-c. Compared to the equivalent simulation without foreland (red curve in Figure 5a), the mean elevation of the uplifting region with a 50-km-long foreland (solid curve in Figure 5a) is about ~ 70 m higher as it reaches a steady-state elevation of $\sim$ 470 m.

Sediment deposition in the foreland basin results in a progressive increase of its slope up to a threshold, over which the sediment flux coming from the uplifting region bypasses the foreland. This steady-state slope varies over the foreland, and the mean slope of the foreland is ~ 0.0032 ($\sum_{i=1}^{N_f} S_i/N_f$, where N_f is the number of foreland nodes, solid curve in Figure 5c), typical of fans built by shallow to deep braided channelized flows (*Stanistreet and McCarthy*, 1993). Many studies of sedimentary fans (*Guerit et al.*, 2014; *Reitz and Jerolmack*, 2012; *Van Dijk et al.*, 2009) have shown that the surface slope stabilizes after some time, which is considered as the steady-state morphology of the fan. In many experimental studies, the fan slope stabilizes quickly because its apex is fixed. Stabilization also occurs if the apex is uplifted through time as the mountain front eventually reaches a steady-state elevation (*Densmore et al.*, 2007). In our simulations, the slope tends to stabilize after several Myr when the mean elevation of the uplifting region has reached steady state.

4.2.2 Sensitivity analysis

In the following, we explore the impact of several parameters such as different foreland lengths, uplift rates, precipitation rates, and different erosion coefficients for bedrock and sediments. The values used for the sensitivity analysis are summarized in Table 1.

In Figure 5, we first assess the effect of foreland length by running four simulations with foreland length of 50 km (the reference simulation, solid curve), 100 km (dashed curve), 200 km (dotted curve), and 300 km (dash-dotted curve), respectively. U is set to 0.2 mm/yr, p to 1 m/yr, G to 1, and K_f to 2×10^{-5} m$^{0.2}$/yr. The maximum thickness of foreland sediments for larger foreland length is higher than the reference simulation (Figure 5b). The sediment thickness in foreland imposes the local base level of the mountain range. Thus, the mean elevation of the uplifting region for larger foreland length is higher than the reference simulation (Figure 5a). However, in the foreland, the mean slopes are significantly lower than the reference simulation (Figure 5c), as they are related to the length of the foreland basin. In fact, sediments are allowed to deposit everywhere until they reach the edge of the domain. Therefore, for a given amount of sediments, the larger the foreland basin, the lower the slope of the foreland basin. This behavior is observed because in our model, rivers are always able to transport sediments even across a large foreland basin.

In Figure 4a, the slope of the fan varies over the 50-km-long foreland, and the fan surface is concave up. We performed several simulations with smaller foreland lengths (5 km, 10 km, and 20 km) in Figure 6. The predicted foreland thickness scales directly with the foreland length (Figure 6). The simulations also show that the fan surface is relatively straight when the foreland length is small (e.g., 5 km). The reduction in fan slope could be due to the reduction in the ratio between the sediment flux q_s and the water flux q_w. The larger the foreland length, the larger the reduction in q_s/q_w downstream, and the more curved the fan surface, as observed in km-scale fans (e.g., *Bull*, 1964; *Densmore et al.*, 2007).

We test for the impact of the uplift rate by running three simulations with $U = 0.2, 0.5$ and 1 mm/yr, respectively. Basin length is set to 50 km, p to 1 m/yr, G to 1,

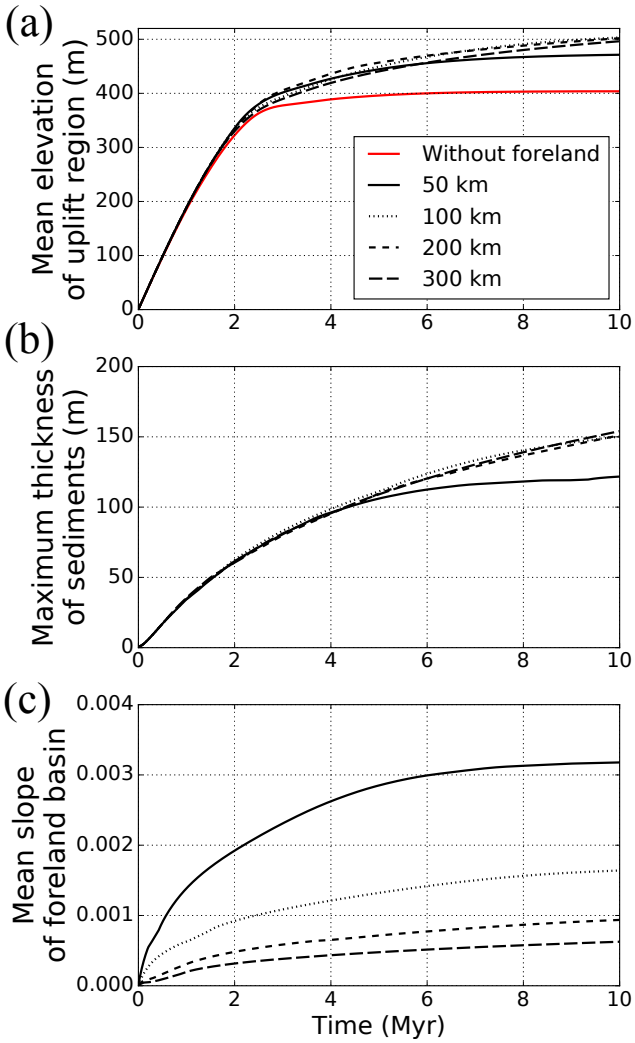

Figure 5. (a) Mean elevation of the uplifting region without foreland, and with foreland length of 50 km, 100 km, 200 km, and 300 km. (b) Maximum thickness of sediments in foreland, and (c) mean slope of the foreland basin as a function of time for foreland length of 50 km, 100 km, 200 km, and 300 km. U is set to 0.2 mm/yr, p to 1 m/yr, G to 1, and K_f to 2×10^{-5} $m^{0.2}$/yr.

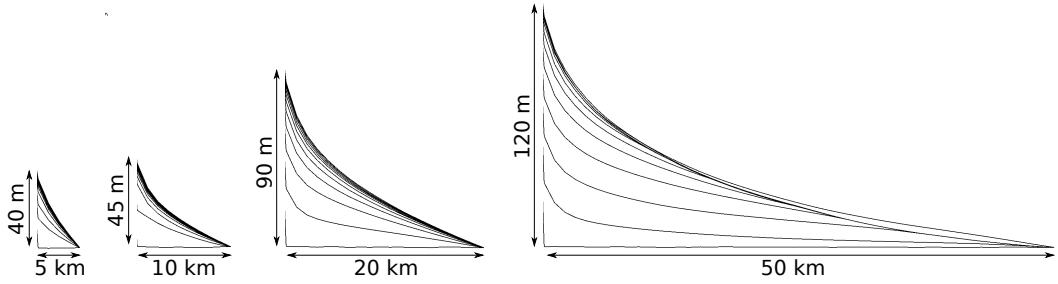

Figure 6. Longitudinal profile of the central foreland topography for various of foreland lengths. Fan surface is relatively straight when the foreland length is small (e.g., 5 km), and is concave up when the foreland length is large ($\geq$ 10 km), consistent with field observations (*Bull*, 1964; *Densmore et al.*, 2007).

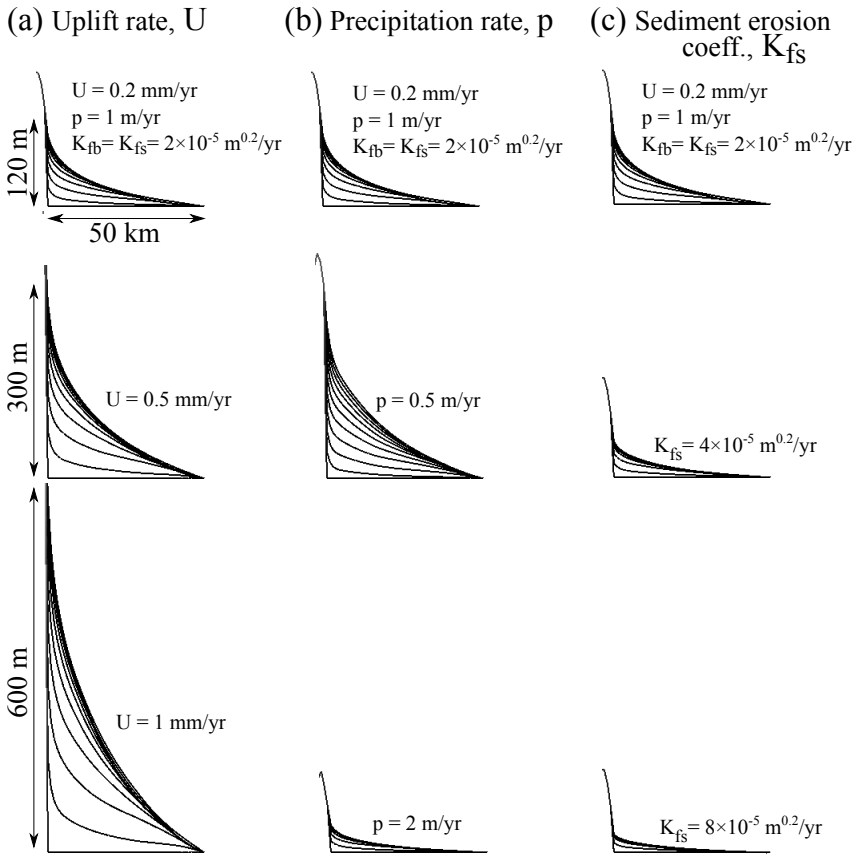

Figure 7. Modelled output for foreland basin showing sensitivity tests on (a) uplift rate U, (b) precipitation rate p, and (c) sediment erosion coefficient K_{fs}. First row shows the standard simulation with the same values throughout. All figures have the same vertical scale.

and K_f to 2×10^{-5} m$^{0.2}$/yr. The main impact of an increased uplift rate is a higher steady-state elevation in the uplifting region. In fact, according to equation (28), the steady-state elevation in the uplifting region is proportional to $U^{1/n}$. The increase in sediment accumulation is also a direct result of the increase in sediment flux resulting from a higher uplift rate. In consequence, sediments can accumulate more in the foreland, and the outlets of the drainage basins are significantly higher (up to 600 m for $U = 1$ mm/yr compared to $\sim$ 120 m for the reference simulation, Figure 7a).

We then test for the impact of precipitation rate by running three simulations with $p = 0.5, 1$, and 2 m/yr, respectively. Basin length is set to 50 km, U to 0.2 mm/yr, G to 1, and K_f to $2{\times}10^{-5}$ m$^{0.2}$/yr. We observe that the higher the precipitation rate p, the lower the foreland deposition and the foreland slope (Figure 7b). This is due to the fact that the erosion rate is proportional to $\tilde{p}^m$ in equation (11), but the deposition term is inversely proportional to $\tilde{p}$, thus, the net deposition rate is proportional to $1/\tilde{p}^{1-m}$. This implies that at higher precipitation rates, the transit of sediments in the foreland is faster (i.e., bypass is more efficient).

Finally, we test for the impact of the erosion coefficient, K_f. In these simulations, we consider different values for the bedrock (K_{fb}) and the sediment (K_{fs}) erosion coefficients. We run three simulations with K_{fb} =$2{\times}10^{-5}$ m$^{0.2}$/yr and $K_{fs} = 2 \times 10^{-5}$, $4{\times}10^{-5}$ and $8{\times}10^{-5}$ m$^{0.2}$/yr, respectively. Basin length is set to 50 km, p to 1 m/yr, and G to 1. As the erosion coefficient increases, sediments in the foreland are more and more remobilized by river erosion, resulting in lower slopes in the foreland basin (Figure 7c). Almost no sediments are preserved in the simulation of $K_{fs} = 8{\times}10^{-5}$ m$^{0.2}$/yr. This means that the reworking (by erosion) of sediments in the foreland is an efficient process that enhances the bypass of sediments from the uplifting region toward the base level.

5 Discussion

5.1 Slope-area ($S - A$) relationship from simulations

By deriving equation (24), we have shown that the inclusion of depositional processes should increase the steepness index, k_s, with respect to the classic SPL model (i.e., with $G = 0$) while the concavity should remain unchanged. This is illustrated by the slope-area analysis of two experiments without foreland with $G = 0$ and $G = 1$ (Figure 3c). With $n = 1$, the concavity and the steepness index can be derived from log-log plots, where the slope of the slope-area relationship is the concavity and the intercept with the origin is the $\log_{10}$ of the steepness index. The slope-area analysis of the simulations $G = 0$ and $G = 1$ reveals a concavity of 0.4 in both experiments, as we expect from our m and n values (0.4 and 1, respectively). On the contrary, despite similar U and K_f, the steepness index k_s is increased by a factor 2 when $G = 1$ (Figure 3c). Through these numerical experiments, we confirm that the steepness index, usually used to derive information about uplift and landscape properties, is also sensitive to the amount of deposition within the fluvial network.

5.2 Autocyclic aggradation and incision in the foreland

During a simulation, the landscape evolves until it reaches an equilibrium topography (when the elevation in the mountain range and the slope in the foreland become stable, Figure 5). In our simulations, river channels continuously migrate laterally in the foreland (Figure 4b, see the animation Movie S3 on water discharge in the Supporting Information), similar to observations made in laboratory experiments (*Van Dijk et al.*, 2009) and other numerical simulations (*Croissant et al.*, 2017; *Pepin et al.*, 2010). By considering the axial topography (Figure 4a; the corresponding animation Movie S2 is presented in the Supporting Information), we can indeed observe that the foreland steady-

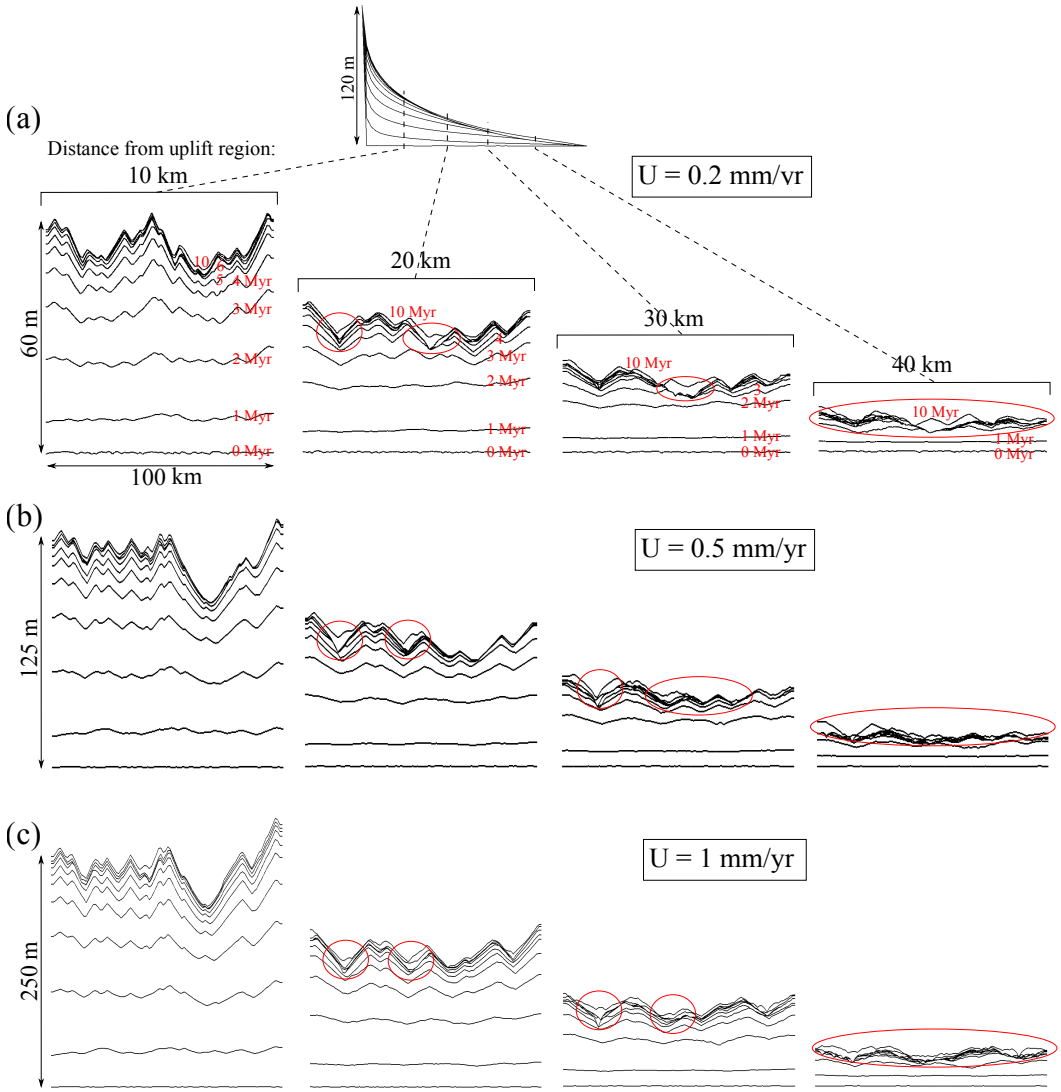

Figure 8. Foreland cross sections at 10 km, 20 km, 30 km, and 40 km from the mountain front for the uplift rate (a) $U = 0.2$ mm/yr, (b) $U = 0.5$ mm/yr, and (c) $U = 1$ mm/yr. Animation of the simulation Movie S4 for aggradation and incision cycles in foreland (a) is presented in the Supporting Information. Red ellipses show the general locations of autocyclic aggradation and incision around a dynamic steady state.

state configuration is a dynamic steady state with the continuous formation and destruction of river banks. The formation and destruction of river banks can be observed from the foreland sections parallel to the mountain front (Figure 8a; the corresponding animation Movie S4 is presented in the Supporting Information). The successive cycles of aggradation and incision mainly occur in the lower foreland (30 km and 40 km in Figure 8a) where the longitudinal slope is low. In the upper foreland, where the slope is higher (10 km and 20 km in Figure 8a), sediments mainly aggrade until reaching steady state. This can be seen, for example, in Figure 4a where sediments aggrade up to a maximum of ~ 120 m at the fan apex (i.e., along the transition between the foreland and the uplifting region). Yet, the amplitude of aggradation and incision is higher close to the mountain range than in the lower foreland, in good agreement with *Bull* (1964).

The successive aggradation and incision cycles arises from the competition between the SPL erosion term $K_f \tilde{p}^m A^m S^n$ and the deposition term $\frac{G}{\tilde{p}A}\int_A \left(U - \frac{\partial h}{\partial t}\right) dA$ in equation (11) where the uplift rate $U = 0$ mm/yr in the foreland. When the foreland slope S is low, the erosion term $K_f \tilde{p}^m A^m S^n$ is lower than the deposition term $\frac{G}{\tilde{p}A}\int_A \left(U - \frac{\partial h}{\partial t}\right) dA$. Then, sediments accumulate in the foreland (because sediments are deposited more than eroded), resulting in an increase of the foreland slope. However, when the foreland slope S is sufficiently large, the erosion term becomes greater than the deposition term, leading to a decrease in slope. The SPL erosion and deposition terms are never equal to each other in the foreland, and a dynamic steady state develops characterized by autocyclic and alternating phases of aggradation and incision.

Note that the node spacing in the simulation is 1×1 km^2 (Figure 8a). To capture morphological features such as valleys and hillslopes that typically occur over shorter space scales, we ran two other simulations with a higher spatial resolution of 100 m and 20 m (Figure S1 in the Supporting Information). The model is smaller (15×10 km^2) than the reference simulation, and has an uplifted domain of 10×10 km^2. The processes that lead to the autocyclic aggradation and incision are replicated (Figure S1), and the spacing between valleys and the migration frequency of river channels are not affected by the spatial resolution of the model.

Langston et al.'s (2015) simulations show that the repeated aggradation and abandonment of high surfaces take place in the upper foreland due to modulation of sediment supply associated with climate change. Unlike their simulations, ours show that, without changing external forcings, streams migrate and sometimes erode into the sediment they have previously deposited, mainly in the lower foreland, around a dynamic steady state. Under a constant forcing, we observe that the upper foreland is quite stable. This could be related to the relatively limited numbers of outlets at the edges of the mountain range, which limits the possibility of major fluvial reworking close to the range.

Riverbed aggradation and incision cycles are often interpreted to reflect changing external forcings including tectonics (*Bull*, 1991; *Yanites et al.*, 2010), climate (*Bridgland and Westaway*, 2008; *Hancock and Anderson*, 2002), and base-level change (*Fisk et al.*, 1945). Yet, without varying tectonics (e.g., the value of U) or climate (e.g., the value of p), our numerical simulations continuously produce lateral migration of river channels in the foreland, resulting in autocyclic aggradation and incision around a dynamic steady state. Using different uplift rates (e.g., $U = 0.5$ mm/yr and 1 mm/yr in Figures 8b and 8c, respectively), we observe larger aggradation and incision thicknesses, because sediments accumulate more in the foreland for higher uplift rates.

5.3 Limitations of the model

There are several limitations to this model and how it can be used to represent natural processes. First of all, our model of course encompasses some limitations of the classic SPL model from which it is derived and such limitations should be considered to design future studies. For example, we can not account for river width variations or lat-

eral migration in bedrock channel, preventing the simulations of alluvial terraces within uplifted areas (*Langston and Tucker*, 2018). Channel narrowing and widening also influence the stream power per unit width, and therefore the transport capacity (e.g., *Finnegan et al.*, 2005; *Whittaker et al.*, 2007).

Second, the thickness and location of deposited sediments above bedrock elevation is not recorded, as erosion and deposition are calculated within the same equation and at the same time step. A valuable addition to this work would be to track sediment deposition within uplifting regions, either within channels or alongside channels in the form of terraces. The transient sediment storage in inter-montane basins or within uplifting regions could be a potential application to better understand landscape evolution. For this, the thickness of sediments above bedrock elevation should be tracked during landscape evolution (e.g., *Shobe et al.*, 2017).

In addition, the model is built in fluxes and it does not account for grain-size distribution (i.e., the eroded material behaves as a single grain-size material). Accordingly, we neither distinguish between bedload and suspended load, nor simulate processes such as sediment downstream fining. The size of the sediments is an important parameter that partly controls the shape and the geometry of sedimentary bodies such as alluvial fans (*Armitage et al.*, 2011; *Delorme et al.*, 2016; *Paola et al.*, 1992). Multiple grain sizes can be incorporated into the model framework by splitting the flux into different loads associated with different deposition coefficients. This would also require to track grain size, which is not trivial to perform in *Davy and Lague*'s (2009) flux-based formulation.

Last, the model did not account for flexural isostasy either in the uplifted domain or in the foreland, mostly for the sake of simplicity, to explain the behavior of the surface process model, independent of any assumption regarding isostatic response. Flexural subsidence of foreland basins creates accommodation space and allows sediments supplied from the uplifted relief to be preserved through time. To simulate sediment stratigraphy with the current model, a first-order approximation would be to impose a negative uplift in the foreland basin to simulate subsidence and enhance sediment deposition and preservation.

6 Conclusion

We have developed a new efficient (i.e., $O(N)$ and implicit) method to solve the equations arising from *Davy and Lague*'s (2009) formulation to investigate the role of sediment deposition on fluvial erosion of landscapes. In our implementation, the deposition rate is assumed to be inversely proportional to drainage area, and proportional to the local suspended sediment flux (estimated from the integrated upstream net erosion rate) and to a dimensionless deposition coefficient, which we term G. This deposition coefficient G is a function of the sediment concentration ratio in transport, the settling velocity of sediment, and the mean precipitation rate. From a macro point of view, $G/\tilde{p}$ in equation (11) is a direct measure of the local deposition rate relative to the mean net erosion rate of upstream drainage area.

To study the behavior of this new scheme and its numerical implementation, we performed a series of simple experiments in which a region subject to uplift at a constant rate is adjacent to a stable area. Based on multiple simulations, we demonstrate that the relief in the uplifting area and the stratigraphy in the foreland basin are controlled by the river erosion coefficient K_f and by the value of G. The deposition coefficient G controls the average elevation in the uplifting region and the surface slope in the associated foreland basin, especially when the value of G is ≥ 1. At steady state, the slope, the average elevation along river profiles and the response time of the uplifted relief are a factor $(1 + G/\tilde{p})^{1/n}$ higher than those derived from the SPL model without a deposition term.

In our simulations, as uplift and erosion progress, sediments aggrade in the foreland basin and prograde toward the foreland edge (the base level). The foreland slope increases until it reaches a threshold over which sediments bypass the foreland. The foreland then develops a dynamic steady state, in which the stream continuously migrates and sometimes cuts into the sediment it has previously deposited. This process leads to the continuous formation and destruction of river banks. This behavior mainly takes place in the lower foreland where the slope is low, whereas in the upper foreland where the slope is relatively high and rivers are less free to migrate, the sediments mainly aggrade until reaching steady state. This observed dynamic steady state suggests that aggradation and incision cycles can occur in the absence of variations in external forcings such as tectonics, climate or change of base level.

As our method is optimally efficient (i.e., $O(N)$ and implicit), it is therefore highly suitable for performing large numbers of simulations and it can thus be used in optimization procedures that require many simulations to infer the amplitude of variations in tectonic forcings, climatic events or base-level changes in natural examples. In the future, we plan on developing this model to better constrain the nature and timing of erosional events on continents, through an inversion of the stratigraphy of the adjacent foreland basins.

A Matrix of finite difference equations in FastScape stack order

To illustrate our algorithm, we now explicitly write the coefficients of matrix $\underline{\underline{B}}$ and vectors $\underline{h}^{t+\Delta t}$ and $\underline{b}^t$ in equation (17) for a single catchment made of 11 nodes (Figure 1c) using the FastScape stack order. This gives:

$$\underline{\underline{B}} = \begin{pmatrix} 1 & 0 & 0 & 0 & 0 & 0 & 0 & 0 & 0 & 0 & 0 \\ -F_2 & 1+F_2 & G/(\tilde{p}\tilde{A}_2) & G/(\tilde{p}\tilde{A}_2) & G/(\tilde{p}\tilde{A}_2) & G/(\tilde{p}\tilde{A}_2) & 0 & 0 & 0 & 0 & 0 \\ 0 & -F_3 & 1+F_3 & G/(\tilde{p}\tilde{A}_3) & G/(\tilde{p}\tilde{A}_3) & 0 & 0 & 0 & 0 & 0 & 0 \\ 0 & 0 & -F_4 & 1+F_4 & 0 & 0 & 0 & 0 & 0 & 0 & 0 \\ 0 & 0 & -F_5 & 0 & 1+F_5 & 0 & 0 & 0 & 0 & 0 & 0 \\ 0 & -F_6 & 0 & 0 & 0 & 1+F_6 & 0 & 0 & 0 & 0 & 0 \\ -F_7 & 0 & 0 & 0 & 0 & 0 & 1+F_7 & G/(\tilde{p}\tilde{A}_7) & G/(\tilde{p}\tilde{A}_7) & G/(\tilde{p}\tilde{A}_7) & G/(\tilde{p}\tilde{A}_7) \\ 0 & 0 & 0 & 0 & 0 & 0 & -F_8 & 1+F_8 & 0 & 0 & 0 \\ 0 & 0 & 0 & 0 & 0 & 0 & -F_9 & 0 & 1+F_9 & G/(\tilde{p}\tilde{A}_9) & G/(\tilde{p}\tilde{A}_9) \\ 0 & 0 & 0 & 0 & 0 & 0 & 0 & 0 & -F_{10} & 1+F_{10} & 0 \\ 0 & 0 & 0 & 0 & 0 & 0 & 0 & 0 & -F_{11} & 0 & 1+F_{11} \end{pmatrix}, \tag{A.1}$$

$$\underline{h}^{t+\Delta t} = \begin{pmatrix} h_1^{t+\Delta t} \\ h_2^{t+\Delta t} \\ h_3^{t+\Delta t} \\ h_4^{t+\Delta t} \\ h_5^{t+\Delta t} \\ h_6^{t+\Delta t} \\ h_7^{t+\Delta t} \\ h_8^{t+\Delta t} \\ h_9^{t+\Delta t} \\ h_{10}^{t+\Delta t} \\ h_{11}^{t+\Delta t} \end{pmatrix}, \quad \text{and} \quad \underline{b}^t = \begin{pmatrix} h_1^t \\ h_2^t + U\Delta t + G(h_3^t + h_4^t + h_5^t + h_6^t + 4U\Delta t)/(\tilde{p}\tilde{A}_2) \\ h_3^t + U\Delta t + G(h_4^t + h_5^t + 2U\Delta t)/(\tilde{p}\tilde{A}_3) \\ h_4^t + U\Delta t \\ h_5^t + U\Delta t \\ h_6^t + U\Delta t \\ h_7^t + U\Delta t + G(h_8^t + h_9^t + h_{10}^t + h_{11}^t + 4U\Delta t)/(\tilde{p}\tilde{A}_7) \\ h_8^t + U\Delta t \\ h_9^t + U\Delta t + G(h_{10}^t + h_{11}^t + 2U\Delta t)/(\tilde{p}\tilde{A}_9) \\ h_{10}^t + U\Delta t \\ h_{11}^t + U\Delta t \end{pmatrix}. \tag{A.2}$$

Let's now take node 2 (the second row in equation A.1) as an example (Figure 1c). Its receiver is node 1 thus there is the term $-F_2 = -K_f \tilde{p}^m A_2^m \Delta t/\Delta l_2$ in the second row of the first column of the matrix $\underline{\underline{B}}$. The node 2 has several upstream nodes (node 3, node

4, node 5, and node 6) which contribute the drainage water, thus, there are dimensionless terms $G/(\tilde{p}\tilde{A}_2)$ in the the second row of the third to the sixth column of the matrix $\underline{\underline{B}}$.

The matrix $\underline{\underline{B}}$ is split into its lower $\underline{\underline{F}}$ and strictly upper triangular matrix $\underline{\underline{E}}$ as:

$$\underline{\underline{F}} = \begin{pmatrix} 1 & 0 & 0 & 0 & 0 & 0 & 0 & 0 & 0 & 0 & 0 \\ -F_2 & 1+F_2 & 0 & 0 & 0 & 0 & 0 & 0 & 0 & 0 & 0 \\ 0 & -F_3 & 1+F_3 & 0 & 0 & 0 & 0 & 0 & 0 & 0 & 0 \\ 0 & 0 & -F_4 & 1+F_4 & 0 & 0 & 0 & 0 & 0 & 0 & 0 \\ 0 & 0 & -F_5 & 0 & 1+F_5 & 0 & 0 & 0 & 0 & 0 & 0 \\ 0 & -F_6 & 0 & 0 & 0 & 1+F_6 & 0 & 0 & 0 & 0 & 0 \\ -F_7 & 0 & 0 & 0 & 0 & 0 & 1+F_7 & 0 & 0 & 0 & 0 \\ 0 & 0 & 0 & 0 & 0 & 0 & -F_8 & 1+F_8 & 0 & 0 & 0 \\ 0 & 0 & 0 & 0 & 0 & 0 & -F_9 & 0 & 1+F_9 & 0 & 0 \\ 0 & 0 & 0 & 0 & 0 & 0 & 0 & 0 & -F_{10} & 1+F_{10} & 0 \\ 0 & 0 & 0 & 0 & 0 & 0 & 0 & 0 & -F_{11} & 0 & 1+F_{11} \end{pmatrix}, \tag{A.3}$$

and

$$\underline{\underline{E}} = \begin{pmatrix} 0 & 0 & 0 & 0 & 0 & 0 & 0 & 0 & 0 & 0 & 0 \\ 0 & 0 & G/(\tilde{p}\tilde{A}_2) & G/(\tilde{p}\tilde{A}_2) & G/(\tilde{p}\tilde{A}_2) & G/(\tilde{p}\tilde{A}_2) & 0 & 0 & 0 & 0 & 0 \\ 0 & 0 & 0 & G/(\tilde{p}\tilde{A}_3) & G/(\tilde{p}\tilde{A}_3) & 0 & 0 & 0 & 0 & 0 & 0 \\ 0 & 0 & 0 & 0 & 0 & 0 & 0 & 0 & 0 & 0 & 0 \\ 0 & 0 & 0 & 0 & 0 & 0 & 0 & 0 & 0 & 0 & 0 \\ 0 & 0 & 0 & 0 & 0 & 0 & 0 & 0 & 0 & 0 & 0 \\ 0 & 0 & 0 & 0 & 0 & 0 & 0 & G/(\tilde{p}\tilde{A}_7) & G/(\tilde{p}\tilde{A}_7) & G/(\tilde{p}\tilde{A}_7) & G/(\tilde{p}\tilde{A}_7) \\ 0 & 0 & 0 & 0 & 0 & 0 & 0 & 0 & 0 & 0 & 0 \\ 0 & 0 & 0 & 0 & 0 & 0 & 0 & 0 & 0 & G/(\tilde{p}\tilde{A}_9) & G/(\tilde{p}\tilde{A}_9) \\ 0 & 0 & 0 & 0 & 0 & 0 & 0 & 0 & 0 & 0 & 0 \\ 0 & 0 & 0 & 0 & 0 & 0 & 0 & 0 & 0 & 0 & 0 \end{pmatrix}. \tag{A.4}$$

Acknowledgments

The work is part of the COLORS project funded by TOTAL. We thank John Armitage, Fiona Clubb, an anonymous reviewer, Associate Editor Mikael Attal, and Editor John M. Buffington for their helpful reviews. We also thank Kim Huppert and Joel Scheingross for the helpful discussions. The codes used for the simulations are available at `https://github.com/fastscape-lem/fastscapelib-fortran`.

References

Ahnert, F. (1967), The role of the equilibrium concept in the interpretation of landforms of fluvial erosion and deposition, pp. 22–41, L'evolution des versants: Liege, Belgium, Universite de Liege.

Allen, P. A., and P. L. Heller (2011), Dispersal and preservation of tectonically generated alluvial gravels in sedimentary basins, *Tectonics of Sedimentary Basins: Recent Advances*, pp. 111–130.

Armitage, J. J., R. A. Duller, A. C. Whittaker, and P. A. Allen (2011), Transformation of tectonic and climatic signals from source to sedimentary archive, *Nature Geoscience*, *4*(4), 231–235.

Armitage, J. J., T. D. Jones, R. A. Duller, A. C. Whittaker, and P. A. Allen (2013), Temporal buffering of climate-driven sediment flux cycles by transient catchment response, *Earth and Planetary Science Letters*, *369*, 200–210.

Babault, J., S. Bonnet, A. Crave, and J. Van Den Driessche (2005), Influence of piedmont sedimentation on erosion dynamics of an uplifting landscape: An experimental approach, *Geology*, *33*(4), 301–304.

Beaumont, C., P. Fullsack, and J. Hamilton (1992), Erosional control of active compressional orogens, in *Thrust tectonics*, pp. 1–18, Springer.

Braun, J., and M. Sambridge (1997), Modelling landscape evolution on geological time scales: a new method based on irregular spatial discretization, *Basin Research*, *9*(1), 27–52.

Braun, J., and S. D. Willett (2013), A very efficient O(n), implicit and parallel method to solve the stream power equation governing fluvial incision and landscape evolution, *Geomorphology*, *180*, 170–179.

Bridgland, D., and R. Westaway (2008), Climatically controlled river terrace staircases: a worldwide quaternary phenomenon, *Geomorphology*, *98*(3-4), 285–315.

Bull, W. B. (1964), *Geomorphology of segmented alluvial fans in western Fresno County, California*, US Government Printing Office.

Bull, W. B. (1991), *Geomorphic responses to climatic change*, Oxford University Press, New York, United States.

Campforts, B., W. Schwanghart, and G. Govers (2017), Accurate simulation of transient landscape evolution by eliminating numerical diffusion: the ttlem 1.0 model, *Earth Surface Dynamics*, *5*(1), 47.

Carretier, S., P. Martinod, M. Reich, and Y. Goddéris (2016), Modelling sediment clasts transport during landscape evolution, *Earth Surface Dynamics*, *3*, 1221–1254.

Chase, C. G. (1992), Fluvial landsculpting and the fractal dimension of topography, *Geomorphology*, *5*(1-2), 39–57.

Cowie, P. A., A. C. Whittaker, M. Attal, G. Roberts, G. E. Tucker, and A. Ganas (2008), New constraints on sediment-flux–dependent river incision: Implications for extracting tectonic signals from river profiles, *Geology*, *36*(7), 535–538.

Crave, A., and P. Davy (2001), A stochastic "precipiton" model for simulating erosion/sedimentation dynamics, *Computers & Geosciences*, *27*(7), 815–827.

Croissant, T., D. Lague, P. Davy, T. Davies, and P. Steer (2017), A precipiton-based approach to model hydro-sedimentary hazards induced by large sediment supplies in alluvial fans, *Earth Surface Processes and Landforms*, *42*(13), 2054–2067.

Davy, P., and D. Lague (2009), Fluvial erosion/transport equation of landscape evolution models revisited, *Journal of Geophysical Research: Earth Surface*, *114*(F03007), 10.1029/2008JF001146.

Delorme, P., V. Voller, C. Paola, O. Devauchelle, É. Lajeunesse, L. Barrier, and F. Métivier (2016), Self-similar growth of a bimodal laboratory fan, *Earth Surface Dynamics*.

Densmore, A. L., P. A. Allen, and G. Simpson (2007), Development and response of a coupled catchment fan system under changing tectonic and climatic forcing, *Journal of Geophysical Research - Earth Sciences*, *112*(F1), {10.1029/2006JF000474}.

Finnegan, N. J., G. Roe, D. R. Montgomery, and B. Hallet (2005), Controls on the channel width of rivers: Implications for modeling fluvial incision of bedrock, *Geology*, *33*(3), 229–232.

Fisk, H. N., et al. (1945), *Geological investigation of the alluvial valley of the lower Mississippi River*, MRC print.

Ganti, V., M. P. Lamb, and B. McElroy (2014), Quantitative bounds on morphodynamics and implications for reading the sedimentary record, *Nature communi-*

cations, *5*, 3298.

Guerit, L., F. Métivier, O. Devauchelle, E. Lajeunesse, and L. Barrier (2014), Laboratory alluvial fans in one dimension, *Physical Review E*, *90*(2), 022,203.

Guerit, L., X. P. Yuan, S. Carretier, S. Bonnet, S. Rohais, J. Braun, and D. Rouby (2018), Macro-scale calibration of sediment deposition coefficient from experimental and natural fluvial landscapes, *pers. comm.*

Hack, J. T. (1957), *Studies of longitudinal stream profiles in Virginia and Maryland*, vol. 294, US Government Printing Office.

Hancock, G. S., and R. S. Anderson (2002), Numerical modeling of fluvial strath-terrace formation in response to oscillating climate, *Geological Society of America Bulletin*, *114*(9), 1131–1142.

Howard, A. D., and G. Kerby (1983), Channel changes in badlands, *Geological Society of America Bulletin*, *94*(6), 739–752.

Johnson, J. P., K. X. Whipple, L. S. Sklar, and T. C. Hanks (2009), Transport slopes, sediment cover, and bedrock channel incision in the henry mountains, utah, *Journal of Geophysical Research: Earth Surface*, *114*(F02014), 10.1029/2007JF000862.

Kooi, H., and C. Beaumont (1994), Escarpment evolution on high-elevation rifted margins: Insights derived from a surface processes model that combines diffusion, advection, and reaction, *Journal of Geophysical Research: Solid Earth*, *99*(B6), 12,191–12,209.

Lacey, G. (1930), Stable channels in alluvium, in *Minutes of the Proceedings of the Institution of Civil Engineers*, vol. 229, pp. 259–292, Thomas Telford-ICE Virtual Library.

Lague, D. (2014), The stream power river incision model: evidence, theory and beyond, *Earth Surface Processes and Landforms*, *39*(1), 38–61.

Lague, D., A. Crave, and P. Davy (2003), Laboratory experiments simulating the geomorphic response to tectonic uplift, *Journal of Geophysical Research: Solid Earth*, *108*(B1), 10.1029/2002JB001785,.

Langston, A. L., and G. E. Tucker (2018), Developing and exploring a theory for the lateral erosion of bedrock channels for use in landscape evolution models, *Earth Surface Dynamics*, *6*(1), 1–27.

Langston, A. L., G. E. Tucker, and R. S. Anderson (2015), Interpreting climate-modulated processes of terrace development along the Colorado Front Range using a landscape evolution model, *Journal of Geophysical Research: Earth Surface*, *120*(10), 2121–2138.

Lavé, J., and J. Avouac (2001), Fluvial incision and tectonic uplift across the himalayas of central nepal, *Journal of Geophysical Research: Solid Earth*, *106*(B11), 26,561–26,591.

Leopold, L. B., and J. P. Miller (1956), *Ephemeral streams: Hydraulic factors and their relation to the drainage net*, vol. 282, US Government Printing Office.

Limaye, A., and M. P. Lamb (2016), Numerical model predictions of autogenic fluvial terraces and comparison to climate change expectations, *Journal of Geophysical Research: Earth Surface*, *121*(3), 512–544, 10.1002/2014JF003392.

Malatesta, L. C., J. P. Prancevic, and J.-P. Avouac (2017), Autogenic entrenchment patterns and terraces due to coupling with lateral erosion in incising alluvial channels, *Journal of Geophysical Research: Earth Surface*, *122*(1), 335–355.

Montgomery, D., and W. Dietrich (1992), Channel initiation and the problem of landscape scale, *Science*, *255*(5046), 826–830.

Montgomery, D. R., and K. B. Gran (2001), Downstream variations in the width of bedrock channels, *Water Resources Research*, *37*(6), 1841–1846, 10.1029/2000WR900393.

Morisawa, M. E. (1962), Quantitative geomorphology of some watersheds in the Appalachian Plateau, *Geological Society of America Bulletin*, *73*(9), 1025–1046.

650 Mouchené, M., P. van der Beek, S. Carretier, and F. Mouthereau (2017), Auto-
651 genic versus allogenic controls on the evolution of a coupled fluvial megafan-
652 mountainous catchment system: numerical modelling and comparison with
653 the lannemezan megafan system (northern pyrenees, france), *Earth Surface*
654 *Dynamics*, *5*(1), 125.
655 Paola, C., and V. Voller (2005), A generalized Exner equation for sediment mass
656 balance, *Journal of Geophysical Research: Earth Surface*, *110*(F04014),
657 10.1029/2004JF000274.
658 Paola, C., P. Hellert, and C. Angevine (1992), The large-scale dynamics of grain-size
659 variation in alluvial basins, 1: Theory, *Basin Research*, *4*(), 73–90.
660 Peaceman, D. W., and H. H. Rachford, Jr (1955), The numerical solution of
661 parabolic and elliptic differential equations, *Journal of the Society for in-*
662 *dustrial and Applied Mathematics*, *3*(1), 28–41.
663 Pepin, E., S. Carretier, and G. Hérail (2010), Erosion dynamics modelling in a cou-
664 pled catchment–fan system with constant external forcing, *Geomorphology*,
665 *122*(1-2), 78–90.
666 Perron, J. T., J. W. Kirchner, and W. E. Dietrich (2009), Formation of evenly
667 spaced ridges and valleys, *Nature*, *460*(7254), 502–505.
668 Reitz, M. D., and D. J. Jerolmack (2012), Experimental alluvial fan evolution:
669 Channel dynamics, slope controls, and shoreline growth, *Journal of Geophysi-*
670 *cal Research: Earth Surface*, *117*(F02021), 10.1029/2011JF002261.
671 Shobe, C. M., G. E. Tucker, and K. R. Barnhart (2017), The space 1.0 model: a
672 landlab component for 2-d calculation of sediment transport, bedrock erosion,
673 and landscape evolution, *Geoscientific Model Development*, *10*(12), 4577–4604.
674 Sklar, L., and W. E. Dietrich (1998), *River Longitudinal Profiles and Bedrock Inci-*
675 *sion Models: Stream Power and the Influence of Sediment Supply*, pp. 237–260,
676 American Geophysical Union, 10.1029/GM107p0237.
677 Sklar, L. S., and W. E. Dietrich (2001), Sediment and rock strength controls on river
678 incision into bedrock, *Geology*, *29*(12), 1087–1090.
679 Stanistreet, I., and T. McCarthy (1993), The Okavango fan and the classification of
680 subaerial fan systems, *Sedimentary Geology*, *85*(1-4), 115–133.
681 Stock, J. D., and D. R. Montgomery (1999), Geologic constraints on bedrock river
682 incision using the stream power law, *Journal of Geophysical Research: Solid*
683 *Earth*, *104*(B3), 4983–4993.
684 Tucker, G. E., and R. L. Slingerland (1994), Erosional dynamics, flexural isostasy,
685 and long-lived escarpments: A numerical modeling study, *Journal of Geophysi-*
686 *cal Research: Solid Earth*, *99*(B6), 12,229–12,243.
687 Van Dijk, M., G. Postma, and M. G. Kleinhans (2009), Autocyclic behaviour of fan
688 deltas: an analogue experimental study, *Sedimentology*, *56*(5), 1569–1589.
689 Walcott, R., and M. Summerfield (2009), Universality and variability in basin outlet
690 spacing: implications for the two-dimensional form of drainage basins, *Basin*
691 *Research*, *21*(2), 147–155.
692 Whipple, K. X. (2001), Fluvial landscape response time: How plausible is steady-
693 state denudation?, *American Journal of Science*, *301*(4-5), 313–325.
694 Whipple, K. X., and G. E. Tucker (1999), Dynamics of the stream-power river in-
695 cision model: Implications for height limits of mountain ranges, landscape
696 response timescales, and research needs, *Journal of Geophysical Research*,
697 *104*(B8), 17,661–17,674.
698 Whipple, K. X., and G. E. Tucker (2002), Implications of sediment-flux-dependent
699 river incision models for landscape evolution, *Journal of Geophysical Research:*
700 *Solid Earth*, *107*(B2, 2039), 10.1029/2000JB000044.
701 Whittaker, A. C., P. A. Cowie, M. Attal, G. E. Tucker, and G. P. Roberts (2007),
702 Bedrock channel adjustment to tectonic forcing: Implications for predicting
703 river incision rates, *Geology*, *35*(2), 103–106.

Wobus, C., K. Whipple, E. Kirby, N. Snyder, J. Johnson, K. Spyropolou, B. Crosby, and D. Sheehan (2006), Tectonics from topography: Procedures, promise, and pitfalls, *Geological Society of America Special Papers*, *398*, 55–74.

Yanites, B. J., G. E. Tucker, K. J. Mueller, and Y.-G. Chen (2010), How rivers react to large earthquakes: Evidence from central taiwan, *Geology*, *38*(7), 639–642.